Biomass HDO Catalysts Innovation from Atomistic Activity Predictors

Fabian Morteo-Flores, Julien Engel and Alberto Roldan*

Cardiff Catalysis Institute, School of Chemistry, Cardiff University, Main Building, Park Place, Cardiff, CF10 3AT, UK

Keywords: biomass, hydrodeoxygenation, activity, descriptors, scaling relation, DFT

Abstract

Circular economy emphasises the idea of transforming products involving economic growth and improving the ecological system to reduce the negative consequences caused by the excessive use of raw materials. This can be achieved with the use of second-generation biomass that converts industrial and agricultural wastes into bulk chemicals. The use of catalytic processes is essential to achieve a viable upgrade of biofuels from the lignocellulosic biomass. We carried out density functional theory (DFT) calculations to explore the relationship between twelve transition metals (TMs) properties, as catalysts, and their affinity for hydrogen and oxygen, as key species in the valorisation of biomass. The relation of these parameters will define the trends of hydrodeoxygenation (HDO) process on biomass-derived compounds. We found the hydrogen and oxygen adsorption energies in the most stable site have a linear relation with electronic properties of these metals that will rationalise the surfaces ability to bind the biomass-derived compounds and break the C-O bonds. This will accelerate the catalyst innovation for low temperature and efficient HDO processes on biomass derivates, e.g. guaiacol and anisole, among others. Among the monometallic catalysts explored, the scaling relationship pointed out that Ni has a promising balance between hydrogen and oxygen affinities according to the d-band centre and d-band width models. The comparison of the calculated descriptors to the adsorption strength of guaiacol on the investigated surfaces indicate that the d-band properties alone are not best suited to describe the trend. Instead, we found that a linear combination of work function and d-band properties gives significantly better correlation.

Introduction

In the last decades, environmental and sustainability awareness has grown against petroleum and natural gas, the long-established foundations of our modern society [1, 2]. Therefore, renewable alternatives must be developed not only as energy carriers but also as feedstock to produce bulk chemicals. As outlined in the EU Action Plan for the Circular Economy, renewable biomass is a desirable substitute if sourced sustainably or recycled, for example, from industrial and agricultural waste [3]. In this context, highly abundant lignocellulosic biomass has come to the focus of attention [4]. However, the conversion of lignin, which makes up about 25 to 30 % of lignocellulosic biomass [5], to valuable chemicals and fuels remains a challenge. Lignin is a highly complex three-dimensional macromolecule consisting of 4-hydroxyphenyl, guaiacol, and syringyl monolignol units connected by a variety of carbon-carbon and carbon-oxygen linkages [6]. A large number of methods for

*Author for correspondence
(RoldanMartinezA@cardiff.ac.uk)
† Cardiff Catalysis Institute, School of Chemistry,
Cardiff University, Main Building, Park Place,
Cardiff, Wales, CF10 3AT, UK

the cleavage of lignin into smaller units have been developed [7, 8]. Still, the high oxygen content of the resulting products is not desirable to use as biofuels or feedstock for aromatic compounds in the petrochemical industry [9]. An important pathway for the reduction of the oxygen content is the hydrodeoxygenation (HDO) process [10, 11]. In the HDO reaction, oxygen-containing groups, such as for example hydroxy or methoxy groups, are removed from the substrate under reducing conditions (Scheme 1).

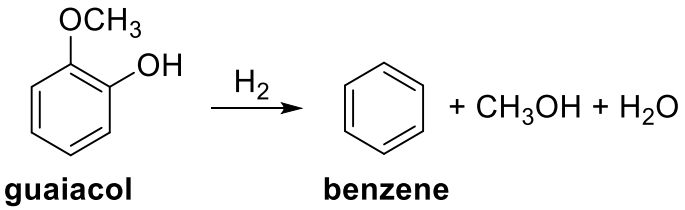

Scheme 1. *Hydrodeoxygenation (HDO) reaction scheme of guaiacol to benzene, water, and methanol.*

As shown by many previous reports, transition metals such as Fe [12, 13], Co [14, 15], Ni [16-18], Cu [16, 19], Mo [20-22], Ru [23, 24], Rh [14, 25], Pd[26-29], W [30], Pt [28, 31-33], or bimetallic combinations such as, AuPd [34], NiFe [7, 35-37], NiCu [38, 39], NiMo [14, 40, 41], and PtNi [31, 42] are highly active catalysts in the HDO reaction. However, these catalysts also show high activity for the hydrogenation of aromatic rings leading to less-desirable saturated products; furthermore, most of these catalysts rapidly deactivate due to coking [25, 43]. A full understanding of the HDO process on the catalysts is of paramount importance for the rational design of new selective and durable catalysts. Several computational studies provided insights into the HDO reaction, but the search for understanding of the relationship between activity, and selectivity and the properties of the catalysts is still ongoing [33, 44-48].

The catalytic activity of supported metal catalysts depends on properties such as structural features (e.g. particle size and shape), the structure and nature of the support, and the intrinsic properties of the metal atoms. For an efficient catalytic turnover, it is not only beneficial to have a thermodynamically feasible pathway with low activation barriers for the desired reaction, but also a weak binding of the products on the catalyst to prevent site inhibition. Commonly, linear Brønsted-Evans-Polanyi (BEP) relationships can be found between the activation and the adsorption energies, which may lead to volcano relations between adsorptions strength and catalytic activity (Sabatier principle) [49-51]. Similar to the BEP, the scaling relationships are graphical constructions illustrating the correlation between adsorption energies, for example of the oxygenated species, and properties of the catalysts, e.g. transition metal surfaces [52]. Basic geometric and electronic properties of

the catalytic surfaces, which, to a great extent, control the activation energies for the elementary surface reaction, can be used as descriptors of the catalytic activity [53, 54]. These descriptors are divided into primary and secondary features. The former ones are derived from the electronic structure, e.g. the d-band centre, d-band width, work function, surface energy, d-band skewness, and kurtosis. While ionisation potential, electron affinity and Pauling electronegativity are secondary features descriptors extracted from the periodic table [55]. Because descriptors are often simple to calculate, extensive screening studies can be carried out efficiently over a wide range of materials accelerating the catalyst innovation [52, 56, 57].

Among the primary features, the surface energy (γ), which corresponds to the energy to create a specific surface from a bulk material, was found to be a suitable descriptor for the catalytic activity of the hydrogen evolution reaction (HER) by Zhuang *et al*. [58]. It is a measure of the degree of coordination on surface atoms. The work function (Φ) indicates the minimum energy necessary to move an electron from the highest occupied band into the vacuum. Losiewicz *et al*. investigated the catalytic activity of different metals in the hydrogen electro-evolution exchange current using the work function as an activity descriptor proving that the catalytic activity is a periodic function of their atomic numbers [59]. Likewise, Shen *et al*. used Φ as an additional descriptor along with the d-band centre to improve the predicting accuracy and to understand the catalytic properties in oxygen reduction reactions [60]. They considered the fact that band hybridisation and electron transfer can occur at the same time when a molecule adsorbs on TMs. The d-band centre (ε_d) parameter was introduced by Hammer and Nørskov [61, 62] and it measures the interaction strength between a TM and an adsorbate, which is directly related to the filling of the bonding orbitals. However, this descriptor needs to explicitly take into account how the bond-strength depends on the reduction of the adsorbate antibonding state, which is defined through the upper-edge position of the d-band [63]. Thus, the emptier the antibonding is, the stronger the interaction becomes. In other words, a higher d-band centre results in stronger bonds [64, 65].

Vojvodic *et al*. proposed a modification of the d-band model introducing the d-band width (W_d) in the oxygen bonding at metal surfaces, $\varepsilon_d^W = \varepsilon_d + W_d/2$ [66]. The new energy descriptor induced variations in bond-strengths, which were not captured by the simple d-band model [67]. The use of these parameters captures the effect of the d-electrons and the interaction with the adsorbate introducing a refined energy descriptor with ε_d and W_d [68]. Thus, the narrower the bandwidth is, the higher the occupation of these d-band is [69].

Several theoretical investigations have analysed the role of the metals for the HDO process [70-73]. However, these studies are focused on the most popular materials with little consideration of the electronic/geometry properties trends. Herein, we analysed the correlation between relevant adsorption energies of the HDO process and properties of transition metal surfaces evaluating their viability as descriptors for the catalytic activity. The use of statistical tools such as violin plot and linear regression allowed us to increase the accuracy with respect to the relation of the descriptors to the interaction energy.

Computational methods

We have carried out spin-polarised density functional theory (DFT) calculations using VASP (Vienna Ab initio Software Package) code [74] to systematically study the hydrogen and oxygen adsorption on a wide range of transition metal surfaces. The exchange and correlation contributions were calculated using the revised functional of Perdew-Burke-Ernzerhof (rPBE) (see Table S1-S2 in the Supplementary Information) [75]. The core electrons were described using the Projected Augmented Wave (PAW) formalism [76], and a kinetic energy cut-off of 550 eV was defined for the valence electron plane-wave basis set. Long-range interactions were added using Grimme's empirical dispersion correction DFT-D3 [77]. Dipole corrections were employed perpendicular to the metal surfaces upon hydrogen/oxygen adsorption. The Brillouin zone was sampled with a Monkhorst-Pack 13×13×13 k-point grid for bulk calculations and 3×3×1 k-point grid for slab calculations [78]. Isolated molecules were placed in a 20×20×20 Å box to avoid interactions with their periodic image.

In this study, we considered group VI (Mo, W), VIII (Fe, Ru), IX (Co, Rh, Ir), X (Ni, Pd, Pt), and XI (Cu, Ag, Au) metals as potential catalysts for the HDO process. These metals crystallise in a face-centred cubic (fcc) (Ni, Cu, Rh, Pd, Ag, Ir, Pt and Au), body-centred cubic (bcc) (Fe, Mo and W) or hexagonal close packed (hcp) lattice (Co and Ru). Slab models of their low index surfaces were generated with the Atomic Simulation Environment (ASE) based on optimised bulk lattice parameters [79]. We have chosen the (100), (110), and (111) surfaces for the metals with fcc and bcc structure, and the (0001), $(10\bar{1}0)$ and $(11\bar{2}0)$ surfaces for hcp metals. Each slab model consists of five atomic layers, where the top two were relaxed and the bottom three layers were fixed to their bulk positions. To avoid any interaction with the periodic images, we added a vacuum of 15 Å along the z-axis (see Figure S1 in the Supporting Information).

Surface characterisation

The surface energy (γ) of the metal surfaces was calculated using Equation 1 from the total energy of the relaxed slab (E_{slab}^{relax}) and the unrelaxed frozen bulk-terminated slab (E_{slab}^{fix}), the energy per atom of the bulk material (E_{bulk}), and the area A of the newly generated surface area [80, 81].

$$\gamma = \frac{E_{slab}^{relax} - E_{bulk}}{A} - \frac{E_{slab}^{fix} - E_{bulk}}{2A} \quad (Eq. 1)$$

The work function (Φ) is defined as the difference between the energy in the vacuum (E^{vac}) and in the highest occupied band, i.e. the Fermi energy (E_F) (Equation 2) (see Figure S2 in the Supporting Information).

$$\phi = E^{vac} - E_F \ (Eq. 2)$$

The d-band centre (ε_d) is defined as the energy d-state cutting through the middle of all the d-states and it is obtained by halving the integral of the d-band [82]. To obtain the d-band width (W_d), the band was normalised using the Gaussian curve fitting to find the best fit for the series of energy states. Based on the rectangular band model approximation, we took the difference between the lowest energy (W_2) and the higher energy states (W_1) within the region, $W_d = W_1 - W_2$ (see Figure S3 in the Supporting Information) [83]. While the d-band skewness (S_d) and d-band kurtosis (K_d) are based on the measure of symmetry and heavy or light tails of the distribution of the d-band [81].

To study the adsorption of hydrogen and oxygen atoms on inequivalent adsorption sites (see Figure 1), the respective atom was placed at 1.5 Å over the top metal layer of the surface and fully relaxed. For the calculation of the gas phase energies of hydrogen and oxygen, the molecules were placed in a sufficiently large box to avoid spurious interactions with the periodic cells [84]. For the fcc metals, these are on top (T), bridge (B), hollow fcc (fcc), and hollow hcp (hcp) on the (111) surface, on top (T), short bridge (SB), long bridge (LB), and hollow (H) on the (110) surface and on top, bridge, and hollow on the (100) surface. The hollow fcc positions are located over a hollow position of the first subsurface layer, while the hollow hcp positions are over a metal atom of the second layer. For the bcc metals, the sites are on top (T), bridge (B), hollow fcc (fcc), and hollow hcp (hcp) on the (111) surface, on top (T), short bridge (SB), long bridge (LB), and hollow on the (110) surface and on top (T), bridge (B), and hollow (H) on the (100) surface. On the (0001) surface of the hcp metals, we defined the on top

(T), bridge (B), hollow fcc, and hollow hcp positions [85]. For $(10\bar{1}0)$ and $(11\bar{2}0)$, the sites are on top, short bridge (SB), long bridge (LB) and hollow [86]. The adsorption energies (E_{ads}) were calculated with Equation 3 where the $E_{ads/slab}$ is the energy of the adsorbate on the slab, and $E_{adsorbate}$ and E_{slab} are the energies of the free adsorbate (H_2 and O_2) and the clean surface, respectively:

$$E_{ads} = E_{ads/slab} - \left(E_{slab} + \frac{1}{2}E_{adsorbate}\right) \quad (Eq.3)$$

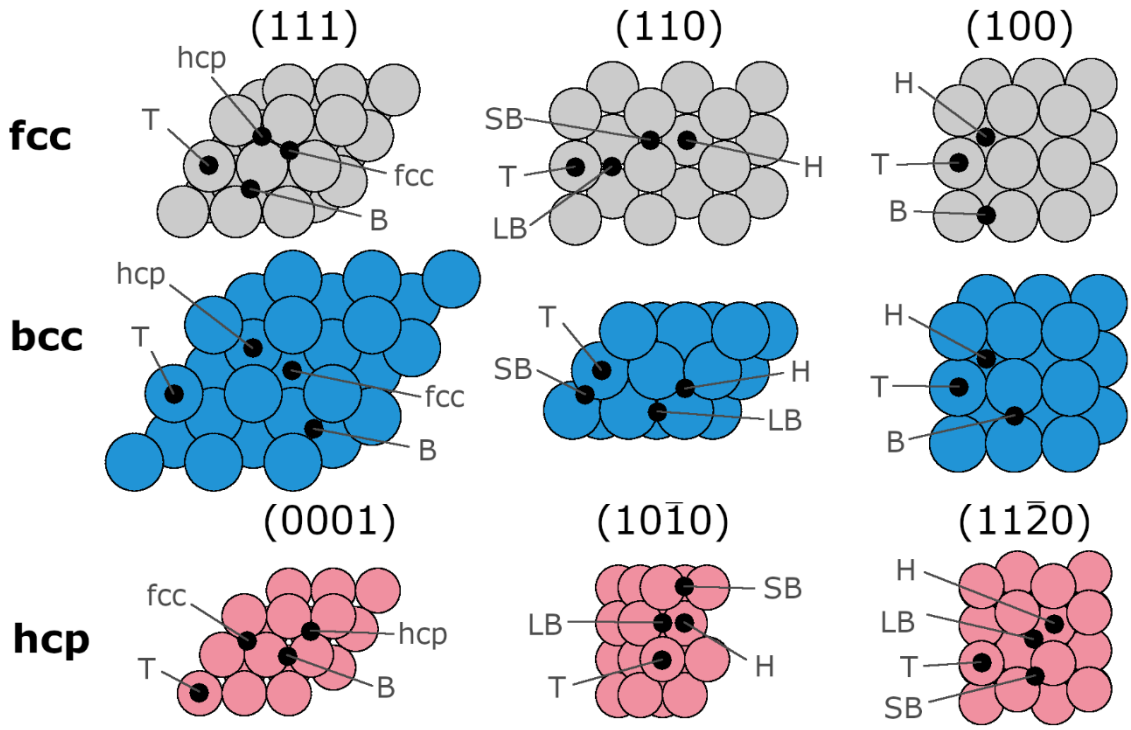

Figure 1. Schematic representations of the different adsorption sites on the (111), (110), and (100) surfaces of Ag (fcc) and W (bcc) and (0001), $(10\bar{1}0)$, and $(11\bar{2}0)$ surfaces of Co (hcp); T: on top; B: bridge; SB: short bridge; LB: long bridge; H: hollow; fcc: hollow position over atom of second layer; hcp: hollow position over hollow position in second layer.

Normalisation (Z-score) is a strategy to transform the data to have a mean of zero and a standard deviation of one allowing to compare and evaluate the accuracy of the descriptors. The Z-score is obtained with equation 4, where x_i is the original data, $\bar{x}$ is the sample mean, and s is the sample standard deviation. This Z-score can be visualised in the violin plot, which allows comparing different sets of data using standardised tables.

$$Z = \frac{x_i - \bar{x}}{s} \qquad (Eq. 4)$$

Results and discussion

We summarised the results on metals optimisation from the bulk-like slab in Table S3 in the Supporting Information. It contains information regarding the areas, the atomic layers distances along the z-axis and slabs magnetisations.

Surface Energy

Our calculated surfaces energies for (111), (110), and (100) surfaces of the fcc (Ni, Cu, Rh, Pd, Ag, Ir, Pt and Au) and bcc metals (Fe, Mo, and W) and (0001), $(10\bar{1}0)$, and $(11\bar{2}0)$ surfaces of the hcp metals (Co and Ru) are shown in Figure 2 [87]. The values obtained are in good agreement with experimental values from previous work with a mean absolute percentage error of 6.5% (see Table S5-S6 in the Supporting Information). We found that the (111) surfaces are the most stable surfaces of the fcc metals due to the higher atomic coordination of the surface atoms compared to the (110) and (100) surfaces. This is in line with previous computational results from Wang *et al*. and Vitos *et al.* obtained with non-spin polarised PBE calculations and LMTO calculations, respectively [88]. Our results, as well as the calculations of Wang *et al.*, indicate a higher stability of the (100) surface compared to the (110) surface for all group X and XI metals and Ir, whereas the results of Vitos *et al.* suggest that the (110) surfaces are more stable for Ni and Pd, and Ir. This trend follows the decrease of the coordination number of the surface layer atoms from (111) (CN: 9) to (100) (CN: 8) and (110) (CN: 7). Interestingly, the (110) surface of Rh is predicted to be slightly more stable (E_{surf} = 0.02 J m^{-2}) than the (100) surface, while both Vitos *et al.* and Wang *et al.* reported the opposite ordering, albeit with small separation of 0.10 and 0.08 J m^{-2}, respectively. The (110) surfaces of group VI metals (Mo and W) are calculated to be most stable followed by the (111) and (100) surfaces in agreement with previous reports. The results of Vitos *et al.* suggest that the (111) surface to be the least stable surface. For the bcc metals, the coordination number of the top layer atoms is not a good indicator of the surface energy as the small difference in distance to first and second neighbours does not properly reflect the density of the packing at the surface. Moreover, we found that the (0001) surfaces of the hcp metals Co and Ru are the most stable surface for these metals, which is in agreement with previous reports [89, 90]. The next most stable surface is in both cases the $(10\bar{1}0)$ surface followed by the $(11\bar{2}0)$ surface. This reflects

the decrease in coordination number of the surface atoms from 9 for the (0001) to 8 for the (10$\bar{1}$0) and 7 for the (11$\bar{2}$0) surface.

The deviations from the mentioned literature values arise from the different computational methodologies, which emphasises the need for a systematic recalculation of the surface energies, here present.

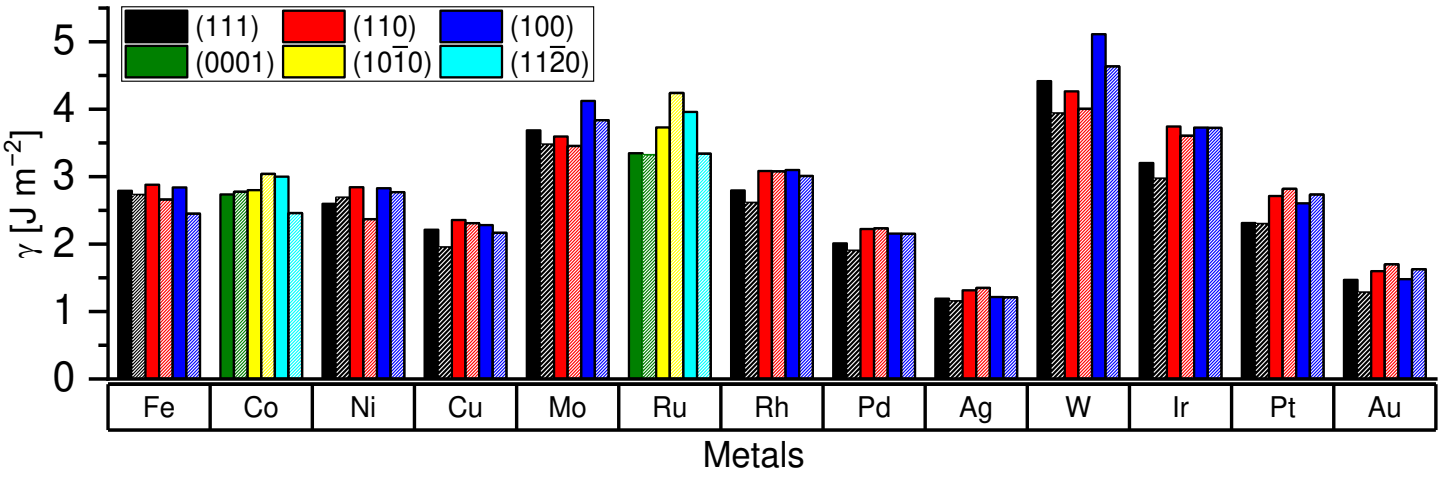

Figure 2. Surface energies (γ) of the investigated metal surfaces. The solid bars represent the herein calculated values whereas the dashed bars represent previous experimental results [88, 90-99].

Higher surface energies are related to surface instability and, therefore, high chemical reactivity. In general, we see a decrease in surface energy within a period with increasing group number. The surfaces of Ag and Au show the lowest surface energies (1.47 and 1.19 J m^{-2}, respectively), which reflects their general low reactivity, whereas the more reactive early transition metals Mo and W have significantly higher values (3.69 and 4.42 J m^{-2}, respectively). Both extremes will lead to a weak catalytic activity according to the Sabatier principle [49-51].

Work Function (Φ)

The work function (Φ) for all investigated metal surfaces is shown in Figure 3. The calculated values for the work function of the surfaces (in Table S7-S8 in the Supporting Information) with a mean absolute percentage error of 4.7% from the experimental values [88, 100]. The work function depends on the exposed metal facet which suggests that the more stable the surface is, the higher the work function becomes. This trend can be confirmed for the fcc metals, where the work function values are in the following order (111) > (100) > (110) for the respective metals. The same sequence can be seen for the bcc metals where the most stable facet (110) has

the highest work function. Higher work function means that the electrons cannot escape easily from the surface because it has a lower probability that the surface is exposed to the vacuum [88]. Therefore, the described trend between work function and surface energy is only valid for surfaces of the same metal and no correlation can be found for the surfaces of different metals [101]. Pt and Ir show the overall highest work function, so it can be concluded that these metals accumulate electron density at the surface while Mo, Fe and W present the lowest work function being poor in electron density at the surfaces [102, 103].

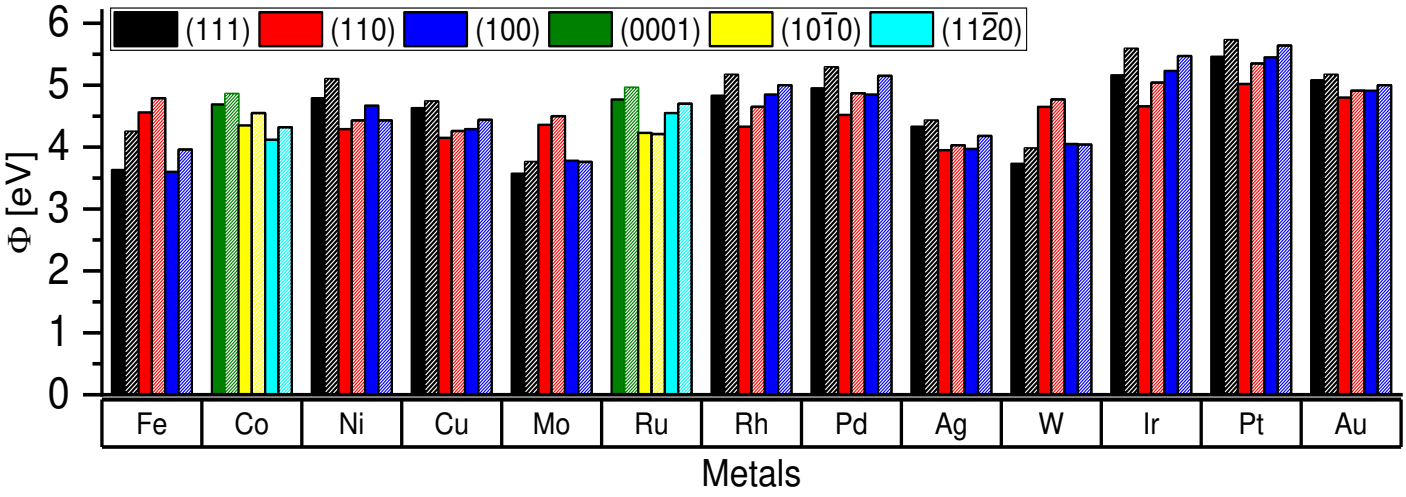

Figure 3. Work function (Φ) of the investigated metal surfaces. The solid bars represents the herein calculated values whereas the dashed bars represent previous experimental results [88, 100].

d-band Properties

We have summarised the calculated values for d-band properties such as: d-band centre (ε_d), width (W_d), skewness (S_d) and kurtosis (K_d) of all metals and surfaces under study as a heatmap in Figure 4-a, 4-b, 4-c, and 4-d respectively.

The herein reported d-band properties have been also calculated by various other studies e. The values of the calculated d-band centre (ε_d) present a mean absolute percentage error of 12.6% with previous works. While there is generally a good agreement with the literature values, the moderate deviation of the percentage error found for the ε_d of the surfaces is due to a considerable difference between the ε_d values of Fe, Pt and Pd (21.3% of mean absolute percentage error). A detailed comparison to previous computational works for ε_d and W_d can be found in Tables S9 and S10 in the Supporting Information, respectively. As expected, the values of the d-

band centres of the most stable surfaces become generally more negative within a period with increasing atomic number due to the increased filling of the d-band except for the group X metals (Ni, Pd, Pt). The d-band centre of the group IX metals (Co, Rh, Ir) is located closer to the Fermi energy than the neighbouring group VIII (Fe, Ru, Os) and group X metals. For example, the d-band centre of Fe(111) was calculated as −1.20 eV while the ones of Co(0001) and Ni(111) are −1.50 eV and −1.42 eV, respectively. Such behaviour was previously described for Ru-Rh-Pd and Os-Ir-Pt [66, 104]. The reason for this could be the change in crystal structure from one metal to the next, which in itself could influence the location of the d-band centre as shown by our results. For the fcc metals, we found (except for Ag) the most negative d-band centres for the (111) surfaces, which exhibit the highest coordination number, but there is no clear correlation between these two properties. The d-band centre follows the ordering (111) < (100) < (110) for Cu and Au but (111) < (110) < (100) for Rh, Ir, and Pt. For Ni, both the (110) and (100) surfaces have the same values for the d-band centre. The lowest d-band centre for Ag can be found for the (100) surface, but the overall variation between the surfaces is only 0.05 eV. In the case of the bcc structures, Fe(110), Mo and W((111) and (110)) have the lowest d-band centre. There is not a relationship either with the most stable surface or the highest coordination number. Fe, Mo, and W (100) showed the highest d-band centre being Mo(100) and W(100) the least stable surfaces. For hcp structures, the (0001) surface are the most stable and with the highest coordination number and have the lowest d-band centre in comparison with $(10\bar{1}0)$) and $(11\bar{2}0)$ surfaces of the same metals. As in the case of the fcc surfaces, there is no clear connection to the coordination number of the surface atoms visible. A higher ε_d corresponds to lower filling of the antibonding states provoking a strong binding between the metal and adsorbates. This suggests that Au and Ag will be less reactive than Mo and W (Figure 4a).

The W_d values calculated were compared with Vojvodic *et al*. [66], resulting in a mean absolute percentage error of 11.7%. This reflects that the method that we used does not give considerably different results to those obtained using the second moment of the electronic density of states in previous works. W_d did not show a link with the ε_d values calculated; this is caused by an independent relation between the filling of d-band with these two descriptors similar to ref [68]. However, W_d presents a good relationship with K_d and S_d (R^2: 0.892 and 0.934 respectively). The trend shows the K_d and S_d values decreasing with increasing W_d (see Figure S4 in the Supporting Information). K_d measures the spread of the d-band, in which lower values means that the d-band is broader and a more positive ε_d while S_d measures the symmetry of the d-band. Positive S_d values mean that the distribution of the states is more concentrated on the right side of the band and its d-band centre is far away from the E_F. Hence, big positive S_d values mean a narrow d-band and a more negative high d-band. Although

there is a good correlation degree with the ε_d (R^2: 0.636 and 0.700 for K_d and S_d respectively), the highest degree correlation with the d-band width means the lack of relationship with W_d and ε_d.

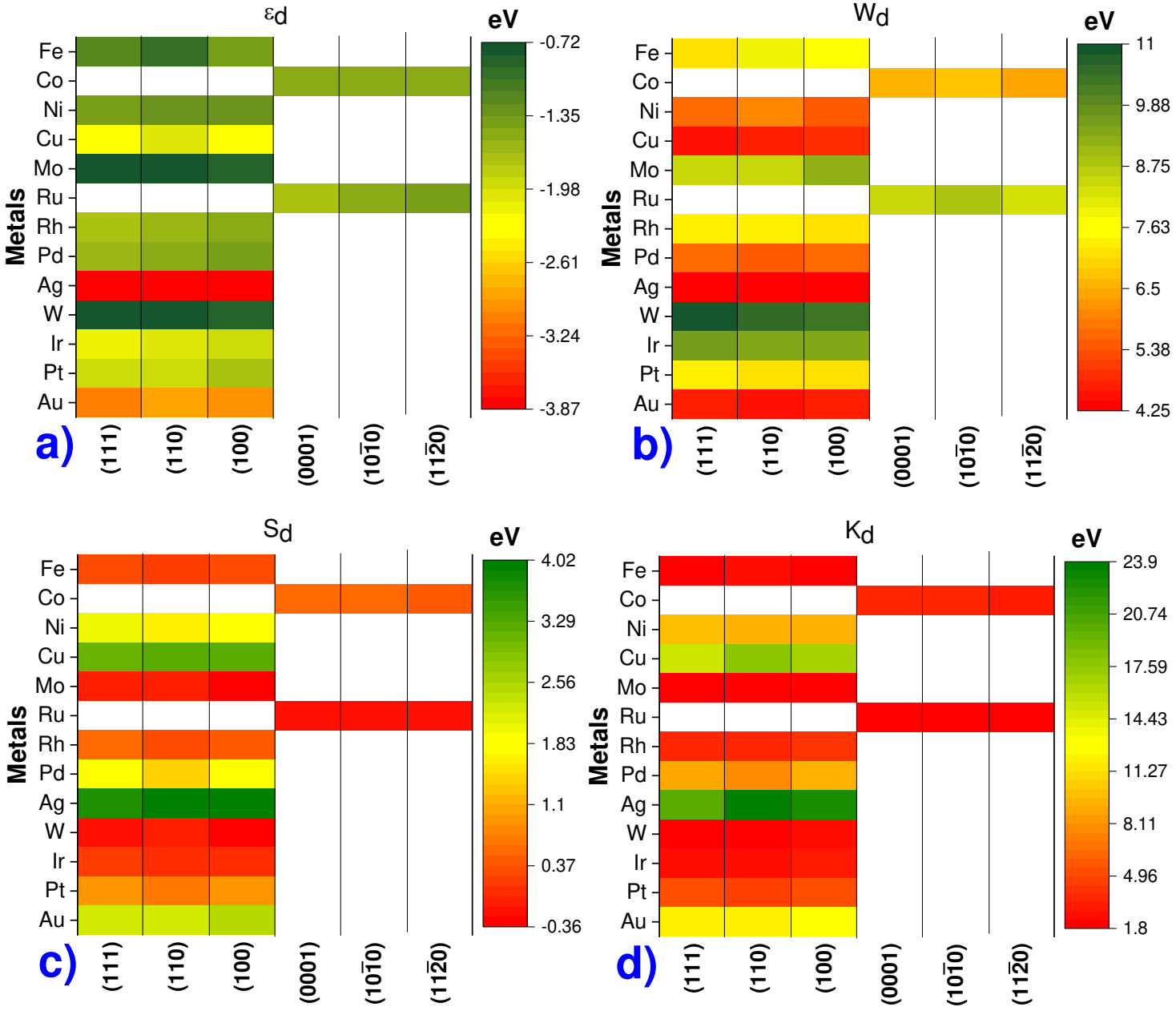

Figure 4. Heatmap of (a) d-band centre (ε_d), (b) d-band width (W_d), (c) d-band skewness (S_d) and (d) d-band Kurtosis (K_d) (in eV) on (111), (110), (100) fcc and bcc and (0001), (10$\bar{1}$0), and (11$\bar{2}$0) hcp surfaces. Smaller

values are given by red colour in the plot. Values are within the range from –3.88 to –0.72 eV for ε_d, 4.25 to 11.0 eV for W_d, –0.36 to 4.02 eV for S_d and 1.80 to 23.90 eV for K_d.

Hydrogen adsorption

We have summarised the hydrogen adsorption energies in a heatmap, see Figure 5 (Table S13-S14 in the Supporting Information for details), which illustrates the dependence on the facet and adsorption site. Except for Pt and Ir, the strongest adsorption of H on the (111) surfaces of the fcc metals was found on hollow sites. The fcc and hcp hollow sites are almost degenerate with a slight preference for the fcc sites on Rh, Pd, and Au and for the hcp sites on Ni. This is in agreement with previous theoretical studies on the adsorption of H on fcc(111) surfaces which suggest that the fcc sites are mostly favoured but without any significant energy difference to the hcp sites [105-117]. According to our calculations H atoms are most stable on top sites of Pt and Ir, whereas some studies only found the top site to be favoured for Ir [118-122]. Others suggest that the top site is more stable for Pt [123, 124]. However, the energy difference between the top sites and the hollow sites was found to be low [112, 113, 123, 124]. On the fcc(110) surfaces, the bridge adsorption sites (SB or LB) are favoured for all metals except Ir and Pt, for which the top site is more stable. However, the top sites on Pt(110) show only an energy difference of 0.01 eV to the short bridge site. The long bridge sites are favoured for Ni and Pd and the short bridge sites for Cu, Rh, Ag, Ir, and Au but the energy difference between both bridge sites is below 0.1 eV for Ni, Cu, Rh, and Pd. DFT calculations by Shi et al. on the Pt(110) found the short bridge site to be most stable but that H atoms on bridge and top sites coexist at higher coverages [122]. Hydrogen adsorption on the (100) surface is the strongest on the hollow sites of Ni, Cu, and Ag and bridge sites of Rh, Pd, Ir, Pt, and Au. Significant energy differences (>0.1 eV) between the hollow and top sites were found only for Ir and Pt. Previous theoretical works also identified these two sites as the most stable ones but which one of these is favoured changed depending on the specific computational methodology used [107, 111, 120, 125-128].

The most stable adsorption site on the (100) surface of the bcc metals Fe, Mo, and W show is the bridge site as found in previous theoretical studies [107, 129]. Our results indicate that there is no general trend for the sites with the lowest energy for H adsorption on the bcc(111) surfaces. The hollow-hcp sites are most stable on Fe(111), the bridge site on Mo(111) and the top site on W(111). The energy between the top and bridge sites on Mo and W is below 0.05 eV. The hollow sites of the bcc(110) surfaces have the lowest energies for the adsorption of hydrogen in agreement with the literature [107, 112, 124, 130, 131].

The most stable adsorption on the (0001) surfaces of the hcp metals Co and Ru are the hollow hcp sites. Other theoretical studies identified the fcc sites as lowest energy positions but there are no significant energy differences to the hcp sites [107, 131-133]. The adsorption on the bridge sites (SB or LB) for $(10\bar{1}0)$, and $(11\bar{2}0)$ hcp surfaces is preferred, while the top position is least favourably.

The magnitude of the adsorption energies ranges from −1.40 eV (on Ru$(11\bar{2}0)$) to +0.13 eV (on Ag(111)) relative to the clean surface and ½ H_2 molecule. Except for Pt and Au, the (110) surfaces of the fcc metals bind strongest to hydrogen compared to the other facets. For Pt and Au, the (100) surface shows a lower adsorption energy, which is equal to the one on the (111) surface in the case of Au. The weakest adsorption of hydrogen can be found on the (111) surface of Rh, Ag, Ir, and Pt, on the (100) surfaces of Ni, Cu, and Pd and on the (110) surface of Au. Our results suggest that the bcc metals Mo and W bind H strongest on the (110) surfaces and weakest on the (100) surfaces. For the surfaces of Fe, we found the strongest adsorption on the (110) surface and the weakest on the (111) surface, but without any significant energy difference (≤0.03 eV). The $(10\bar{1}0)$, and $(11\bar{2}0)$ surfaces of Ru interact stronger with hydrogen compared to the (0001) surface while the energy difference between these surfaces is not larger than 0.03 eV for Co. On all surfaces except Ag (111), the adsorption energies are negative, which means that the chemisorption of atomic hydrogen is energetically favoured.

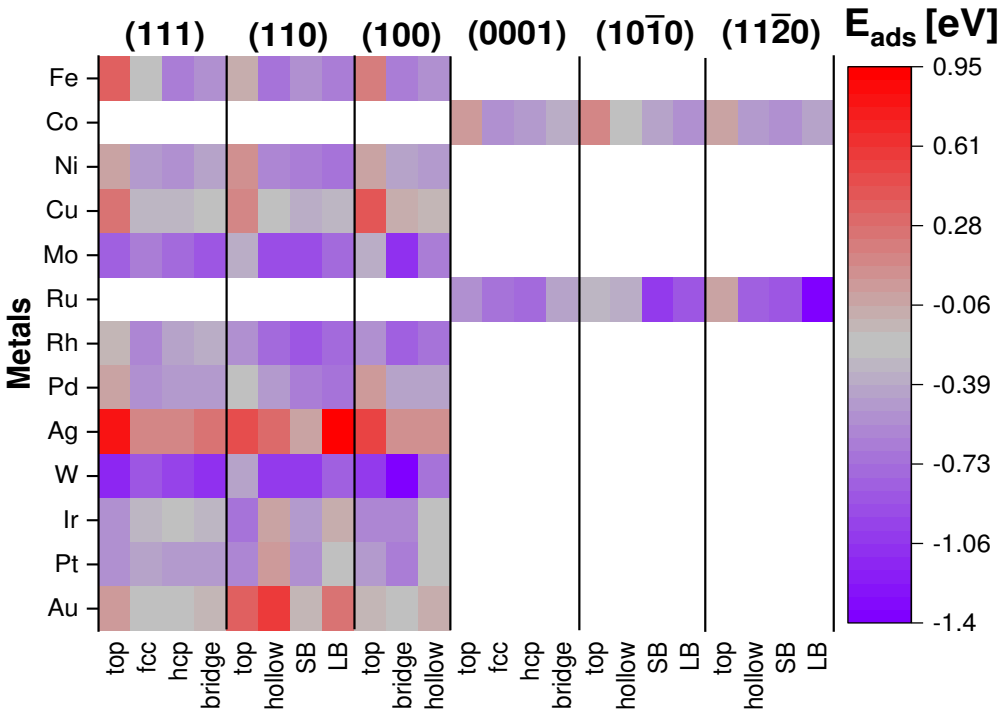

Figure 5. Heatmap of hydrogen adsorption energies (E_{ads}); values within the range from –1.40 to 0.95 eV.

Oxygen adsorption

We have summarised the oxygen adsorption energies in a heatmap, see Figure 6 (see Table S15-S16 in the Supporting Information for details), which illustrates the dependence on the facet and adsorption site. The most favourable adsorption site on the fcc(111) surfaces is the fcc hollow site followed by the hcp site in agreement with previous theoretical works [105, 109, 114, 115, 117, 118, 134-140].

On the fcc(110) surfaces, the short bridge sites are favoured for all metals except Cu and Ag for which the hollow site is more stable. The hollow sites are the lowest energy adsorption sites for oxygen on most of the fcc(100) surfaces as reported in previous publications [126, 128, 141-143]. Only for Ir and Pt, the bridge sites were found to be more stable which is in agreement with other theoretical calculations [144-148]. On the bcc(100) surfaces, the adsorption of oxygen occurs preferentially on the hollow sites of Fe(100) and on the bridge sites of Mo(100) and W(100). This is in agreement with previous computational studies [149-152].

The hollow sites were identified as most stable positions for oxygen adsorption on the (110) surfaces of Fe and W while the long bridge position is most favourable on Mo(110). The results for Fe(110) and W(110) are in good

agreement with the literature [153, 154]. However, the hollow position shows the weakest adsorption for oxygen on Mo(110) whereas previous studies concluded that it would be the most stable site but followed by long bridge site [155-157]. The favoured oxygen adsorption sites on the bcc(111) surfaces are the bridge sites for Fe(111) and Mo(111) and top sites for W(111). As for hydrogen, the favoured positions for oxygen adsorption on the (0001) surfaces of the hcp metals are the hollow-hcp sites closely followed by the fcc sites. This confirms the results found previously by other studies [133, 158-160]. For the $(10\bar{1}0)$ surface, oxygen prefers the long bridge and short bridge sites for Co and Ru, respectively, while on the $(11\bar{2}0)$ surfaces the short bridge sites are favoured for both Co and Ru. In agreement with previous reports, bcc metals have a strong oxyphilic character [161-164], which may facilitate the direct cleavage of C—O bonds but will require elevated temperatures to release the oxygenated compounds. The different behaviour of these facets opens the possibility of nanoparticles engineering where the right ratio between desired facets may enhance the catalytic activity and selectivity towards specific products.

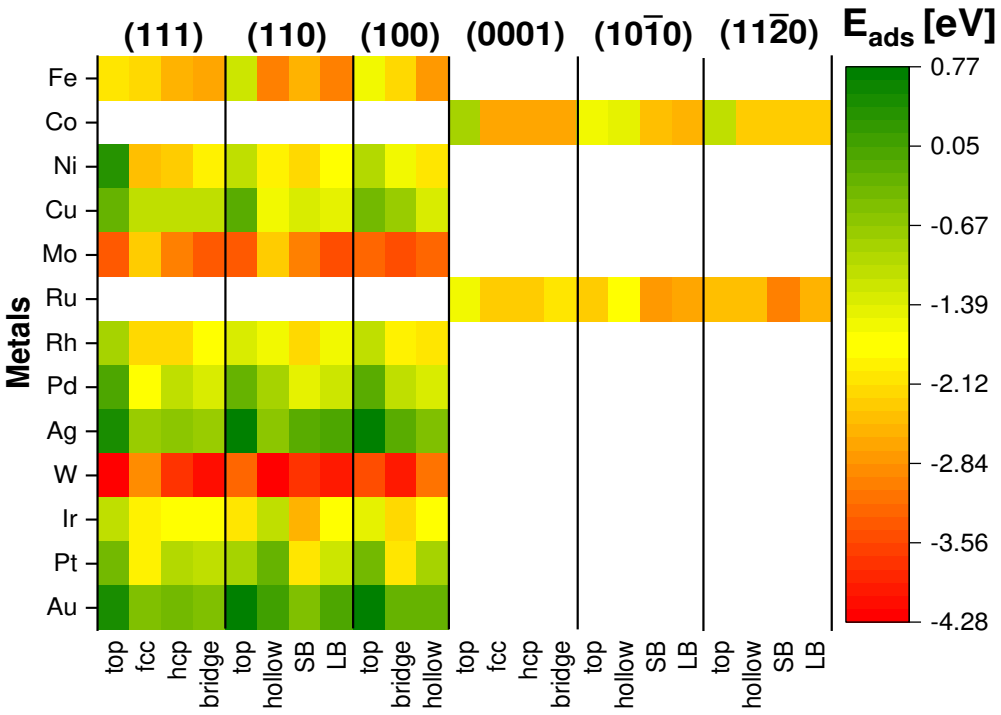

Figure 6. Heatmap of oxygen adsorption energies (E_{ads}); only values within range from −4.28 to 0.77 eV

Scaling relations

To maximise the predictive character of this study, we analysed the trends in hydro- and oxophilicity by exploring several relationships between the adsorption energies and surface descriptors described above. Combining the metals and surfaces explored, we have more than 39 values to normalise (Tables S17-S30 in the Supplementary Information) leading to a violin plot enhancing the comparison and rationalisation. The violin plot, see Figure 7, represents the statistical distribution of the normalised descriptors, which is convenient for comparing them. This plot will help us to visualise the entire distribution of the data and to analyse linear relationships. The more normal distributed, i.e. symmetrical shape with a wide belly curved around zero, is the data, the more likely a linear trendline (and a higher degree of correlation).

We have identified the median of the results of each descriptor, white point in the centre of the violin plots because it is a robust estimate of the mean and ensures the average of the low or high values of it [68]. The distribution of the data shows a bell-shaped curve (Gaussian curve) within Z-score range of −3 to 3, where the mean dominates the position of the centre, i.e. the median and the mean are equal [54]. The data related to the work function (Φ) and d-band centre (ε_d), second and third violin, falls right on the mean although the position is not in the centre, which is determined by the peak of the curve. The d-band width violin presents an elongated distribution without a well-defined peak around the mean indicating a lack of symmetry in the data and, therefore, a weak linear trend. Both the d-band skewness (S_d) and kurtosis (K_d) show the belly-shape curve in one extreme, this is related to a log-normal distribution, in which the data is more skewed in one part (as we can see in Figure S8-S9 in the Supporting information). This will give as a result a better logarithmic trend with the H and O adsorption energies than a linear trend.

The first and the last violins, i.e. surface energy (γ) and d-band width modification ($\varepsilon_d^W = \varepsilon_d + W_d/2$) [66] descriptors, have a defined peak of the curve falling right to the mean. Moreover, their wide sections are remarkably concentrated around the median value, very close to zero Z-score, showing that the data is symmetrically around the mean. This means that these descriptors are within one standard deviation of the mean, hence, there is a high probability to fit in a linear trend with the dataset with a high degree of correlation [165].

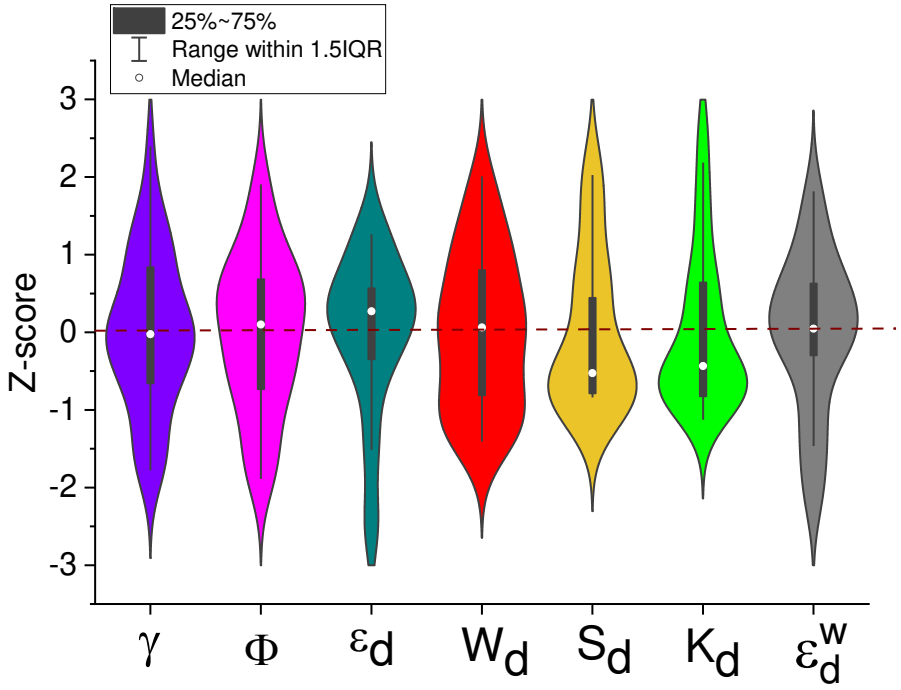

Figure 7. Violin plots of the descriptors surface energy (γ), work function (Φ), d-band centre (ε_d), d-band width (W_d), d-band skewness (S_d), d-band kurtosis (K_d) and d-band width modification (ε_d^W) of the TMs candidates.

The violin plot facilitates the identification of descriptors and based on the information from Figure 7, we have represented scaling relationships between the descriptors and the adsorption energies of the most stable sites (see Figure 8 and Figures S5-S11 in the Supplementary Information). Inset in these figures there are the corresponding (multiple) correlation coefficient (R^2), which is used as a statistical test to measure the association between the two variables i.e. descriptors and adsorption energy [166]. As close to one is R^2 the better is the fitting and stronger the relationship between variables.

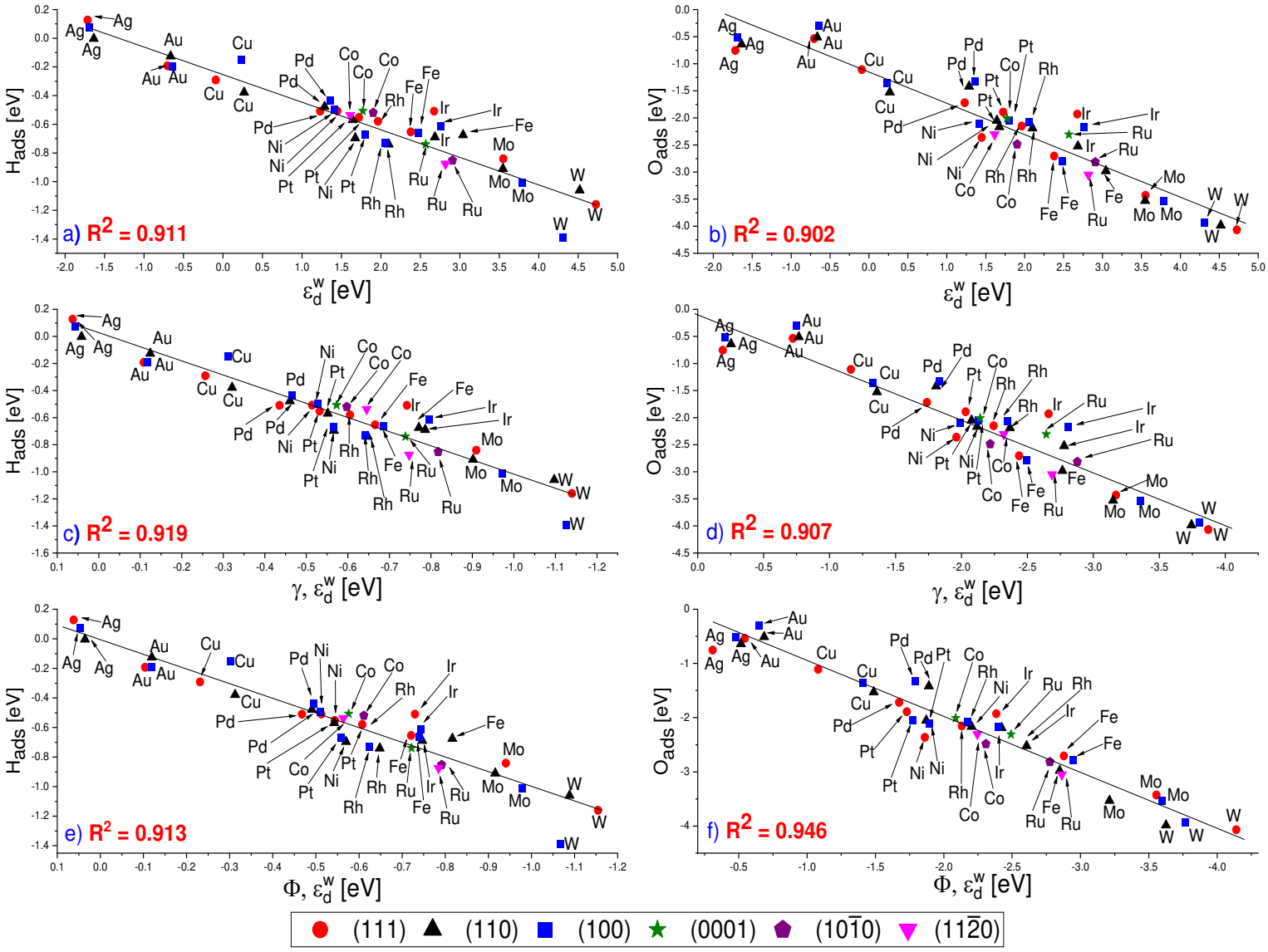

Figure 8. Scaling relationships between (a) d-band width modification (ε_d^W) for (a) H and (b) O adsorption energies, surface energy (γ) with the d-band width modification (ε_d^W) for (c) H and (d) O adsorption energies, and work function (Φ) with the d-band width modification (ε_d^W) for (e) H and (f) O adsorption energies. Simple (a and b) and multiple (c-f) linear regression coefficients (R^2) are inset.

The addition of a second descriptor can increase the correlation between the chemical properties and the affinity of atomic or molecular species [166]. Using a multiple linear regression model ($Y_{calc} = \beta_o + \beta_1 x_1 + \beta_2 x_2$), we created combined descriptors (with x: γ, Φ, ε_d, and W_d; see Supporting Information for details on the fitting). These present a substantial improvement in accuracy correlating both adsorption energies with the combination of ε_d^W

with different descriptors (R^2: 0.919 and 0.907 for γ and R^2: 0.919 and 0.907 for the Φ). It proves that the electron transfer (represented by Φ) between the adsorbent and TM surface and the band hybridisation (represented by ε_d^W) can occur at the same time during the adsorption process [60]. Moreover, it was demonstrated that not only the electronic properties control the catalytic activity but also the stability of the structure related to the measure of the number of bonds broken to form a new surface is a good factor to take into account in the material selection. The charge of H and O on such metal surfaces is quite different and the small magnitude of the fitting parameter β_1 for H adsorption compared to the O adsorption reflects the lower influence of the electron transfer for the H adsorption.

The results herein discussed on metals hydrogen and oxygen affinities and based on Sabatier's principle [49-51], we rationalise the selection of a monometallic HDO catalysts. The scaling relationships with ε_d^W, $\varepsilon_d^W + \gamma$ and $\varepsilon_d^W + \Phi$ gave as a result that Ag and Au have weak affinities for H and O, contrarily to Mo, W, and Ru, which is too strong. Cu, Pd and Pt are considered intermediate weak adsorption energies, while Fe, Rh and Co have intermediate strong adsorption energies. The three models point to Ni as metal catalysts with intermediate affinities for hydrogen and oxygen (neither too strong nor too weak). This outcome is a good agreement with several studies which use Ni as part of metal catalysts such as monometallic, bimetallic supported in hydrogenation and deoxygenation process of biomass derivates with good results [167-169].

Adsorption of Guaiacol

Based on the results of the descriptor calculations, we selected six metal surfaces to study the adsorption of guaiacol (GUA), prominent model substrate for the HDO reaction. More precisely, we investigated the most stable surfaces of Fe, Co, Ni, Cu, Pd, and Pt according to their intermediate adsorption energies of H and O. GUA molecule was placed at different adsorption positions (0°, 45° and 90°) on the TMs selected as shown in Figure 9 (see Table S33).

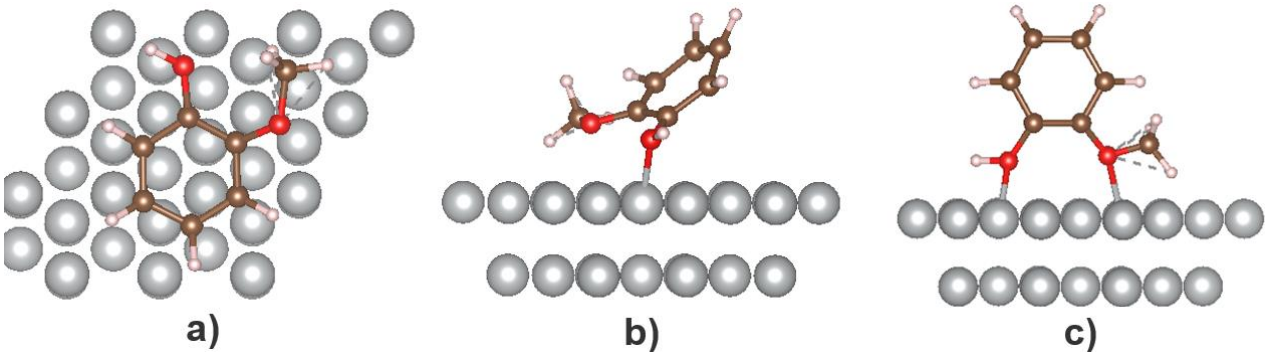

Figure 9. Schematic view of the different adsorption on Ni(111) when the molecule (GUA) is adsorbed in a) parallel (0°), b) 45°and c) perpendicular (90°) form.

As shown in Table 1, the weakest adsorption is at a 90° angle between the surface and the aromatic ring of the substrate, while the strongest is at 0° (Table S33 in the Supporting Information). This is due to the aromatic ring in the guaiacol is characterised by a cloud of π-electrons; these electrons interact strongly with the surfaces increasing the selectivity and adsorption energy. This parallel mode results found in aromatic compounds are similar to those reported for similar surfaces [7, 44, 170-172].

Table 1. Adsorption of guaiacol (GUA) on metals surfaces in different positions.

		Ni (111)	Cu (111)	Pt (111)	Fe (110)	Pd (111)	Co (0001)
E_{ads} [eV]	0°	−1.48	−1.41	−2.11	−1.64	−1.56	−1.47
	45°	−1.31	−0.72	−1.63	−1.25	−1.44	−1.24
	90°	−1.00	−0.87	−1.56	−1.59	−0.78	−0.81

The order of the guaiacol adsorption energy (E_{ads}) is Pt(111) > Fe(110) > Pd(111) > Ni(111) > Co(0001) > Cu(111). We noticed that the trend is almost the same as we found in the scaling relations where Cu(111) and Co(0001) have an intermediate-weak adsorption strength and Fe(110) and Pt(111) have an intermediate-strong adsorption with GUA. Figure 10 shows the guaiacol adsorption energy against the descriptors studied, something to highlight is the strong adsorption found on Pt(111). These results indicate that there is no correlation between the adsorption energy, the surface energy and d-band centre (see Figure 10-a and 10-c). For example, Pt(111) binds the substrate strongest (−1.92 eV) but has the second highest d-band centre. A better correlation can be obtained with the work function as descriptor (see Figure 10-b) although it was identified as a poor descriptor for the adsorption of H and O. An increase in Φ corresponds to an increase in E_{ads}, which is related to the nature

of the surface in terms of charge transfer. For example, Pt accumulates more electron density at the surface than Cu(111), which has smaller work function [101]. This observation makes clear that the selection of materials not only depends on the interaction with the d-band and their properties but also on the metal's nature. The use of different the descriptors Φ, Φ + ε_d, and Φ + ε_d^W gives a linear trend with a high correlation degree (R^2: 0.740, 0.793 and 0.877 eV, respectively) as shown in Figure 10-b, 10-h and 10-i. These indicate the main role of Φ and ε_d^W, which better relate to the strength of the bond on the metals.

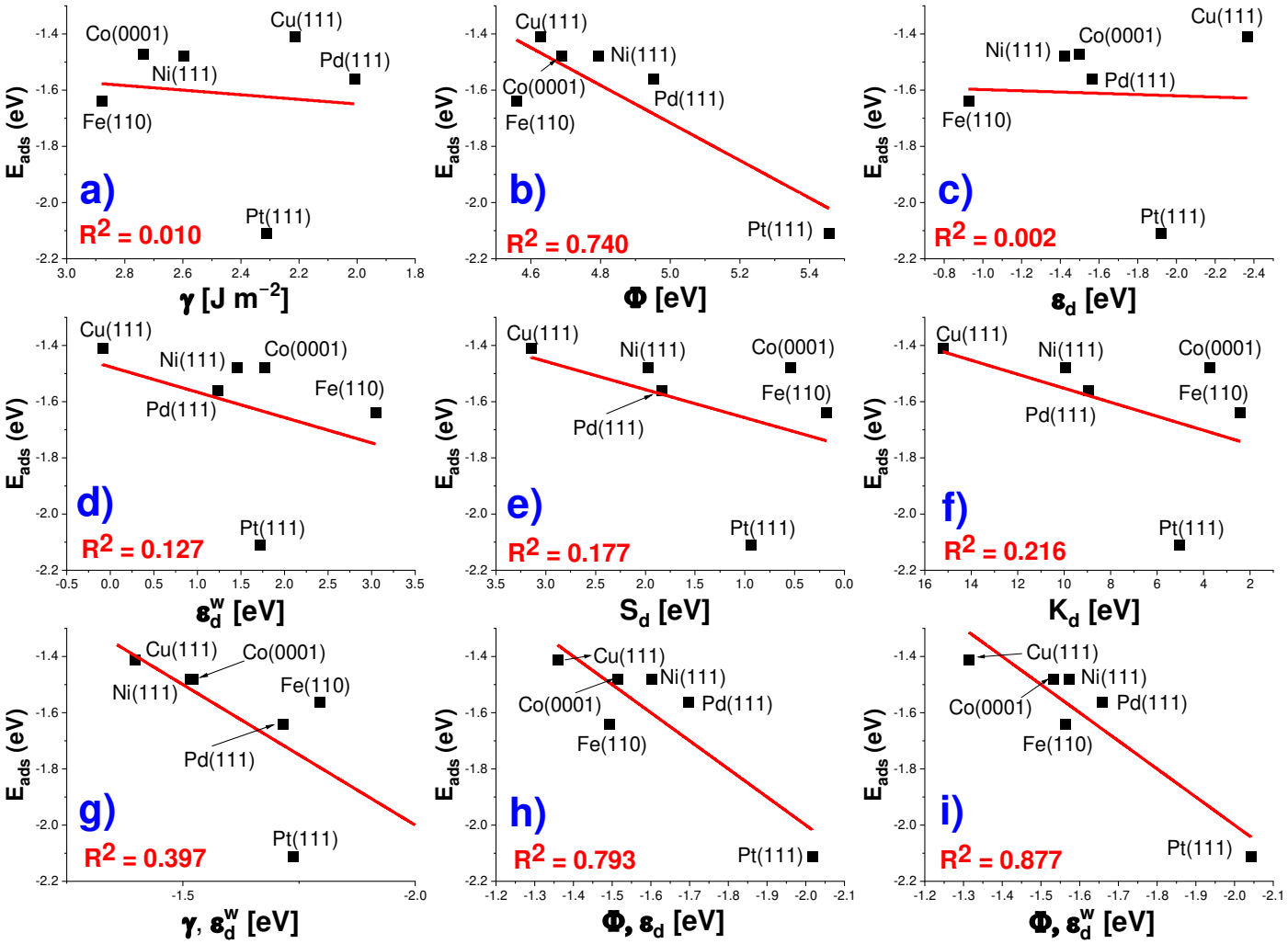

Figure 10. Plots of absorption energy for GUA against the descriptors (a) surface energy (γ), (b) work function (Φ), (c) d-band centre (ε_d), (d) d-band width modification (ε_d^W), (e) d-band skewness (S_d), (f) d-band kurtosis (K_d), (g) surface energy (γ) with the d-band width modification (ε_d^W), (h) work function (Φ) with the d-band

centre (ε_d), and (i) work function (Φ) with the d-band width modification (ε_d^W) of the TMs selected. Linear regression coefficients (R^2) are inset.

Conclusion

The creations of scaling relationships using the adsorption energies of H, O on the surfaces were analysed using GGA-rPBE. The descriptors were evaluated with the violin plot normalising the data in which the surface energy (γ) and the d-band width modification ε_d^W showed a normal distribution which means that they are more likely to fit in a linear regression. This hypothesis was confirmed using these two descriptors in the scaling relationship giving a high R^2 correlation (> 0.85) in both H and O species, providing high accuracy in the selection of the metal surfaces concluding that the ε_d descriptor is not a universal parameter to describe the interactions with the d-band and modification needs to be done to improve the accuracy in the selection of materials.

In the three models studied, Ni is the metal with intermediate affinities for H and O, and therefore good properties for the hydrogenation of oxygenated reactions along the HDO process, this results is in a good agreement with multiple investigations using this metal as monometallic and as a part of bimetallic catalysts supported on different materials [164, 173-175]. Finally, we validated the applicability of our descriptors for the HDO of guaiacol by comparing them to the adsorption energies. The results showed that the work function is an important and valuable descriptor of the adsorption strength of the substrate although it showed no correlation to the adsorption of H and O. The best results were obtained by combining the descriptors of work function and d-band properties. Ultimately, these results help us to build a robust screening methodology for catalytic materials but also shed light on the chemical properties that influence the adsorption and catalytic process.

Additional Information

Information on the following should be included wherever relevant.

Ethics

Insert ethics statement here is applicable

Data Accessibility

All data created during this research are openly available from the University of Cardiff Research Portal
http://doi.org/10.17035/d.2020.0104938086

Authors' Contributions

All authors contributed equally

Competing Interests

There are no conflicts to declare

Funding Statement

Acknowledgments

FM-F gratefully acknowledges to CONACYT (National Council for Science and Technology) for the student scholarship with the reference number 440221. JE would like to thank the Deutsche Forschungsgemeinschaft (DFG) for support through a research fellowship (EN 1229/1-1). UK Catalysis Hub is thanked for resources and support provided through our membership of the UK Catalysis Hub Consortium and funded by the Engineering and Physical Sciences Research Council (EPSRC) (grants EP/K014706/1, EP/K014668/1, EP/K014854/1, EP/K014714/1, and EP/M013219/1). We also thank the EPSRC for the support through the EP/P005845/1 grant. Via our membership of the UK's HEC Materials Chemistry Consortium, which is funded by EPSRC (EP/L000202), this work used the UK Materials and Molecular Modelling Hub for computational resources, MMM Hub, which is partially funded by EPSRC (EP/P020194). We also acknowledge computing time on the facilities of Supercomputing Wales and the Advanced Research Computing @ Cardiff (ARCCA) at Cardiff University

Disclaimer

References

1. Sorrell S, Speirs J, Bentley R, Brandt A, Miller R. Global oil depletion: A review of the evidence. Energy Policy. 2010;38(9):5290-5.
2. Shafiee S, Topal E. When will fossil fuel reserves be diminished? Energy policy. 2009;37(1):181-9.
3. Act SM. Communication from the commission to the European parliament, the council, the economic and social committee and the committee of the regions. 2011.
4. Knauf M, Moniruzzaman M. Lignocellulosic biomass processing: A perspective. International Sugar Journal. 2004;106:147-50.
5. Xu C, Arancon RAD, Labidi J, Luque R. Lignin depolymerisation strategies: towards valuable chemicals and fuels. Chemical Society Reviews. 2014;43(22):7485-500.
6. Zakzeski J, Bruijnincx PC, Jongerius AL, Weckhuysen BM. The catalytic valorization of lignin for the production of renewable chemicals. Chemical reviews. 2010;110(6):3552-99.

7. Liu X, An W, Wang Y, Turner CH, Resasco DE. Hydrodeoxygenation of guaiacol over bimetallic Fe-alloyed (Ni, Pt) surfaces: reaction mechanism, transition-state scaling relations and descriptor for predicting C–O bond scission reactivity. Catalysis Science & Technology. 2018;8(8):2146-58.
8. Dabral S, Engel J, Mottweiler J, Spoehrle SS, Lahive CW, Bolm C. Mechanistic studies of base-catalysed lignin depolymerisation in dimethyl carbonate. Green chemistry. 2018;20(1):170-82.
9. De Wild P, Huijgen W, Kloekhorst A, Chowdari R, Heeres H. Biobased alkylphenols from lignins via a two-step pyrolysis–Hydrodeoxygenation approach. Bioresource technology. 2017;229:160-8.
10. Saidi M, Samimi F, Karimipourfard D, Nimmanwudipong T, Gates BC, Rahimpour MR. Upgrading of lignin-derived bio-oils by catalytic hydrodeoxygenation. Energy & Environmental Science. 2014;7(1):103-29.
11. Morales-Delarosa S, Campos-Martin JM. 6 - Catalytic processes and catalyst development in biorefining. In: Waldron K, editor. Advances in Biorefineries: Woodhead Publishing; 2014. p. 152-98.
12. Hensley AJ, Wang Y, McEwen J-S. Phenol deoxygenation mechanisms on Fe (110) and Pd (111). ACS Catalysis. 2015;5(2):523-36.
13. Hensley AJ, Wang Y, McEwen J-S. Adsorption of guaiacol on Fe (110) and Pd (111) from first principles. Surface Science. 2016;648:227-35.
14. Lin Y-C, Li C-L, Wan H-P, Lee H-T, Liu C-F. Catalytic hydrodeoxygenation of guaiacol on Rh-based and sulfided CoMo and NiMo catalysts. Energy & Fuels. 2011;25(3):890-6.
15. Viljava T-R, Komulainen R, Krause A. Effect of H2S on the stability of CoMo/Al2O3 catalysts during hydrodeoxygenation. Catalysis Today. 2000;60(1-2):83-92.
16. Sitthisa S, Resasco DE. Hydrodeoxygenation of furfural over supported metal catalysts: a comparative study of Cu, Pd and Ni. Catalysis letters. 2011;141(6):784-91.
17. Jin S, Xiao Z, Li C, Chen X, Wang L, Xing J, et al. Catalytic hydrodeoxygenation of anisole as lignin model compound over supported nickel catalysts. Catalysis Today. 2014;234:125-32.
18. Chang J, Danuthai T, Dewiyanti S, Wang C, Borgna A. Hydrodeoxygenation of Guaiacol over Carbon-Supported Metal Catalysts. ChemCatChem. 2013;5(10):3041-9.
19. Dongil A, Bachiller-Baeza B, Rodriguez-Ramos I, Fierro J, Escalona N. The effect of Cu loading on Ni/carbon nanotubes catalysts for hydrodeoxygenation of guaiacol. RSC advances. 2016;6(32):26658-67.
20. Huuska MK. Effect of catalyst composition on the hydrogenolysis of anisole. Polyhedron. 1986;5(1):233-6.
21. Romero Y, Richard F, Brunet S. Hydrodeoxygenation of 2-ethylphenol as a model compound of bio-crude over sulfided Mo-based catalysts: Promoting effect and reaction mechanism. Applied Catalysis B: Environmental. 2010;98(3):213-23.
22. Prasomsri T, Shetty M, Murugappan K, Román-Leshkov Y. Insights into the catalytic activity and surface modification of MoO 3 during the hydrodeoxygenation of lignin-derived model compounds into aromatic hydrocarbons under low hydrogen pressures. Energy & Environmental Science. 2014;7(8):2660-9.
23. Elliott DC, Hart TR. Catalytic Hydroprocessing of Chemical Models for Bio-oil. Energy & Fuels. 2009;23(2):631-7.
24. Boonyasuwat S, Omotoso T, Resasco DE, Crossley SP. Conversion of guaiacol over supported Ru catalysts. Catalysis letters. 2013;143(8):783-91.
25. Gutierrez A, Kaila RK, Honkela ML, Slioor R, Krause AOI. Hydrodeoxygenation of guaiacol on noble metal catalysts. Catalysis Today. 2009;147(3):239-46.
26. Prochazkova D, Zámostný P, Bejblova M, Červený L, Čejka J. Hydrodeoxygenation of aldehydes catalyzed by supported palladium catalysts. Applied Catalysis A: General. 2007;332(1):56-64.
27. Zhao C, He J, Lemonidou AA, Li X, Lercher JA. Aqueous-phase hydrodeoxygenation of bio-derived phenols to cycloalkanes. Journal of Catalysis. 2011;280(1):8-16.
28. Gao D, Schweitzer C, Hwang HT, Varma A. Conversion of Guaiacol on Noble Metal Catalysts: Reaction Performance and Deactivation Studies. Industrial & Engineering Chemistry Research. 2014;53(49):18658-67.

29. Hong Y, Zhang H, Sun J, Ayman KM, Hensley AJR, Gu M, et al. Synergistic Catalysis between Pd and Fe in Gas Phase Hydrodeoxygenation of m-Cresol. ACS Catalysis. 2014;4(10):3335-45.
30. Fang H, Roldan A, Tian C, Zheng Y, Duan X, Chen K, et al. Structural tuning and catalysis of tungsten carbides for the regioselective cleavage of CO bonds. Journal of Catalysis. 2019;369:283-95.
31. Do PTM, Foster AJ, Chen J, Lobo RF. Bimetallic effects in the hydrodeoxygenation of meta-cresol on γ-Al2O3 supported Pt–Ni and Pt–Co catalysts. Green Chemistry. 2012;14(5):1388-97.
32. Peng B, Zhao C, Mejía-Centeno I, Fuentes GA, Jentys A, Lercher JA. Comparison of kinetics and reaction pathways for hydrodeoxygenation of C3 alcohols on Pt/Al2O3. Catalysis Today. 2012;183(1):3-9.
33. Lu J, Behtash S, Mamun O, Heyden A. Theoretical Investigation of the Reaction Mechanism of the Guaiacol Hydrogenation over a Pt(111) Catalyst. ACS Catalysis. 2015;5(4):2423-35.
34. Tuteja J, Nishimura S, Ebitani K. Change in reactivity of differently capped AuPd bimetallic nanoparticle catalysts for selective oxidation of aliphatic diols to hydroxycarboxylic acids in basic aqueous solution. Catalysis Today. 2016;265:231-9.
35. Leng S, Wang X, He X, Liu L, Liu Ye, Zhong X, et al. NiFe/γ-Al2O3: A universal catalyst for the hydrodeoxygenation of bio-oil and its model compounds. Catalysis Communications. 2013;41:34-7.
36. Shafaghat H, Rezaei PS, Daud WMAW. Catalytic hydrodeoxygenation of simulated phenolic bio-oil to cycloalkanes and aromatic hydrocarbons over bifunctional metal/acid catalysts of Ni/HBeta, Fe/HBeta and NiFe/HBeta. Journal of Industrial and Engineering Chemistry. 2016;35:268-76.
37. Fang H, Zheng J, Luo X, Du J, Roldan A, Leoni S, et al. Product tunable behavior of carbon nanotubes-supported Ni–Fe catalysts for guaiacol hydrodeoxygenation. Applied Catalysis A: General. 2017;529:20-31.
38. Bykova MV, Ermakov DY, Kaichev VV, Bulavchenko OA, Saraev AA, Lebedev MY, et al. Ni-based sol–gel catalysts as promising systems for crude bio-oil upgrading: Guaiacol hydrodeoxygenation study. Applied Catalysis B: Environmental. 2012;113-114:296-307.
39. Khromova SA, Smirnov AA, Bulavchenko OA, Saraev AA, Kaichev VV, Reshetnikov SI, et al. Anisole hydrodeoxygenation over Ni–Cu bimetallic catalysts: The effect of Ni/Cu ratio on selectivity. Applied Catalysis A: General. 2014;470:261-70.
40. Ryymin E-M, Honkela ML, Viljava T-R, Krause AOI. Competitive reactions and mechanisms in the simultaneous HDO of phenol and methyl heptanoate over sulphided NiMo/γ-Al2O3. Applied Catalysis A: General. 2010;389(1):114-21.
41. Dabros TMH, Andersen ML, Lindahl SB, Hansen TW, Høj M, Gabrielsen J, et al. Hydrodeoxygenation (HDO) of aliphatic oxygenates and phenol over NiMo/MgAl2O4: reactivity, inhibition, and catalyst reactivation. Catalysts. 2019;9(6):521.
42. Lai Q, Zhang C, Holles JH. Hydrodeoxygenation of guaiacol over Ni@Pd and Ni@Pt bimetallic overlayer catalysts. Applied Catalysis A: General. 2016;528:1-13.
43. Shi D, Arroyo-Ramírez L, Vohs JM. The use of bimetallics to control the selectivity for the upgrading of lignin-derived oxygenates: Reaction of anisole on Pt and PtZn catalysts. Journal of catalysis. 2016;340:219-26.
44. Lee K, Gu GH, Mullen CA, Boateng AA, Vlachos DG. Guaiacol hydrodeoxygenation mechanism on Pt (111): insights from density functional theory and linear free energy relations. ChemSusChem. 2015;8(2):315-22.
45. Dupont C, Lemeur R, Daudin A, Raybaud P. Hydrodeoxygenation pathways catalyzed by MoS2 and NiMoS active phases: A DFT study. Journal of catalysis. 2011;279(2):276-86.
46. Moon J-S, Kim E-G, Lee Y-K. Active sites of Ni2P/SiO2 catalyst for hydrodeoxygenation of guaiacol: A joint XAFS and DFT study. Journal of catalysis. 2014;311:144-52.
47. Verma AM, Kishore N. DFT study on gas-phase hydrodeoxygenation of guaiacol by various reaction schemes. Molecular Simulation. 2017;43(2):141-53.

48. Zhang J, Fidalgo B, Shen D, Zhang X, Gu S. Mechanism of hydrodeoxygenation (HDO) in anisole decomposition over metal loaded Brønsted acid sites: Density Functional Theory (DFT) study. Molecular Catalysis. 2018;454:30-7.
49. Medford AJ, Vojvodic A, Hummelshøj JS, Voss J, Abild-Pedersen F, Studt F, et al. From the Sabatier principle to a predictive theory of transition-metal heterogeneous catalysis. Journal of Catalysis. 2015;328:36-42.
50. Che M. Nobel Prize in chemistry 1912 to Sabatier: Organic chemistry or catalysis? Catalysis today. 2013;218:162-71.
51. Nørskov JK, Bligaard T, Logadottir A, Bahn S, Hansen LB, Bollinger M, et al. Universality in heterogeneous catalysis. Journal of catalysis. 2002;209(2):275-8.
52. Abild-Pedersen F, Greeley J, Studt F, Rossmeisl J, Munter T, Moses PG, et al. Scaling properties of adsorption energies for hydrogen-containing molecules on transition-metal surfaces. Physical review letters. 2007;99(1):016105.
53. Calle-Vallejo F, Koper MT, Bandarenka AS. Tailoring the catalytic activity of electrodes with monolayer amounts of foreign metals. Chemical Society Reviews. 2013;42(12):5210-30.
54. Ghiringhelli LM, Vybiral J, Levchenko SV, Draxl C, Scheffler M. Big data of materials science: critical role of the descriptor. Physical review letters. 2015;114(10):105503.
55. Li Z, Ma X, Xin H. Feature engineering of machine-learning chemisorption models for catalyst design. Catalysis today. 2017;280:232-8.
56. Loffreda D, Delbecq F, Vigné F, Sautet P. Chemo− Regioselectivity in Heterogeneous Catalysis: Competitive Routes for CO and CC Hydrogenations from a Theoretical Approach. Journal of the American Chemical Society. 2006;128(4):1316-23.
57. Van Santen RA, Neurock M, Shetty SG. Reactivity theory of transition-metal surfaces: a Brønsted− Evans− Polanyi linear activation energy− free-energy analysis. Chemical reviews. 2009;110(4):2005-48.
58. Zhuang H, Tkalych AJ, Carter EA. Surface energy as a descriptor of catalytic activity. The Journal of Physical Chemistry C. 2016;120(41):23698-706.
59. Łosiewicz B, Popczyk M, Napłoszek I, Budniok A, editors. Intermetallic Compounds as Catalysts in the Reaction of Electroevolution/Absorption of Hydrogen. Solid State Phenomena; 2015: Trans Tech Publ.
60. Shen X, Pan Y, Liu B, Yang J, Zeng J, Peng Z. More accurate depiction of adsorption energy on transition metals using work function as one additional descriptor. Physical Chemistry Chemical Physics. 2017;19(20):12628-32.
61. Pérez-Mendoza A, Ribadeneira R. Modeling with DFT and Chemical Descriptors Approach for the Development of Catalytic Alloys for PEMFCs. Density Functional Theory: IntechOpen; 2018.
62. Hammer B, Nørskov J. Electronic factors determining the reactivity of metal surfaces. Surface Science. 1995;343(3):211-20.
63. Bhattacharjee S, Waghmare UV, Lee S-C. An improved d-band model of the catalytic activity of magnetic transition metal surfaces. Scientific reports. 2016;6:35916.
64. Hammer B, Norskov JK. Why gold is the noblest of all the metals. Nature. 1995;376(6537):238-40.
65. Medford A, Vojvodic A, Hummelshøj J, Voss J, Abild-Pedersen F, Studt F, et al. ChemInform Abstract: From the Sabatier Principle to a Predictive Theory of Transition-Metal Heterogeneous Catalysis. Journal of Catalysis. 2015;328.
66. Vojvodic A, Nørskov J, Abild-Pedersen F. Electronic structure effects in transition metal surface chemistry. Topics in catalysis. 2014;57(1-4):25-32.
67. Pettifor D. Theory of the crystal structures of transition metals. Journal of Physics C: Solid State Physics. 1970;3(2):367.
68. Pankajakshan P, Sanyal S, de Noord OE, Bhattacharya I, Bhattacharyya A, Waghmare U. Machine learning and statistical analysis for materials science: stability and transferability of fingerprint descriptors and chemical insights. Chemistry of Materials. 2017;29(10):4190-201.

69. Economou EN. The physics of solids: essentials and beyond: Springer Science & Business Media; 2010.
70. Garcia-Pintos D, Voss J, Jensen AD, Studt F. Hydrodeoxygenation of phenol to benzene and cyclohexane on Rh (111) and Rh (211) surfaces: insights from density functional theory. The Journal of Physical Chemistry C. 2016;120(33):18529-37.
71. Verma AM, Kishore N. Molecular simulations of palladium catalysed hydrodeoxygenation of 2-hydroxybenzaldehyde using density functional theory. Physical Chemistry Chemical Physics. 2017;19(37):25582-97.
72. Nelson RC, Baek B, Ruiz P, Goundie B, Brooks A, Wheeler MC, et al. Experimental and theoretical insights into the hydrogen-efficient direct hydrodeoxygenation mechanism of phenol over Ru/TiO2. ACS catalysis. 2015;5(11):6509-23.
73. Luo J, Yun H, Mironenko AV, Goulas K, Lee JD, Monai M, et al. Mechanisms for high selectivity in the hydrodeoxygenation of 5-hydroxymethylfurfural over PtCo nanocrystals. ACS Catalysis. 2016;6(7):4095-104.
74. Kresse G, Furthmüller J. Efficiency of ab-initio total energy calculations for metals and semiconductors using a plane-wave basis set. Computational materials science. 1996;6(1):15-50.
75. Perdew JP, Burke K, Ernzerhof M. Generalized gradient approximation made simple. Physical review letters. 1996;77(18):3865.
76. Blöchl PE. Projector augmented-wave method. Physical review B. 1994;50(24):17953.
77. Grimme S, Antony J, Ehrlich S, Krieg H. A consistent and accurate ab initio parametrization of density functional dispersion correction (DFT-D) for the 94 elements H-Pu. The Journal of chemical physics. 2010;132(15):154104.
78. Monkhorst HJ, Pack JD. Special points for Brillouin-zone integrations. Physical review B. 1976;13(12):5188.
79. Larsen AH, Mortensen JJ, Blomqvist J, Castelli IE, Christensen R, Dułak M, et al. The atomic simulation environment—a Python library for working with atoms. Journal of Physics: Condensed Matter. 2017;29(27):273002.
80. dos Santos Politi JR, Viñes F, Rodriguez JA, Illas F. Atomic and electronic structure of molybdenum carbide phases: bulk and low Miller-index surfaces. Physical Chemistry Chemical Physics. 2013;15(30):12617-25.
81. Xin H, Vojvodic A, Voss J, Nørskov JK, Abild-Pedersen F. Effects of d-band shape on the surface reactivity of transition-metal alloys. Physical Review B. 2014;89(11):115114.
82. Lima FHB, Zhang J, Shao MH, Sasaki K, Vukmirovic MB, Ticianelli EA, et al. Catalytic Activity−d-Band Center Correlation for the O2 Reduction Reaction on Platinum in Alkaline Solutions. The Journal of Physical Chemistry C. 2007;111(1):404-10.
83. Miller S, Dsilva C, Kitchin JR. Coverage dependent adsorption properties of atomic adsorbates on late transition metal surfaces. Catalysis: Volume 24. 24: The Royal Society of Chemistry; 2012. p. 83-115.
84. Zhang L, Goddard III WA, Jiang S. Molecular simulation study of the c (4× 2) superlattice structure of alkanethiol self-assembled monolayers on Au (111). The Journal of chemical physics. 2002;117(15):7342-9.
85. Shang XF, Wang YW, Tao XM, Tan MQ, editors. Hydrogen Chemisorption on Co (0001) Surface: A DFT Study. Advanced Materials Research; 2012: Trans Tech Publ.
86. Vega L, Ruvireta J, Vines F, Illas F. Jacob's ladder as sketched by escher: Assessing the performance of broadly used density functionals on transition metal surface properties. Journal of chemical theory and computation. 2018;14(1):395-403.
87. Spencer MJ, Hung A, Snook IK, Yarovsky I. Density functional theory study of the relaxation and energy of iron surfaces. Surface Science. 2002;513(2):389-98.
88. Wang J, Wang S-Q. Surface energy and work function of fcc and bcc crystals: Density functional study. Surface science. 2014;630:216-24.

89. Zhang J-M, Wang D-D, Xu K-W. Calculation of the surface energy of hcp metals by using the modified embedded atom method. Applied Surface Science. 2006;253(4):2018-24.
90. Vitos L, Ruban A, Skriver HL, Kollar J. The surface energy of metals. Surface science. 1998;411(1-2):186-202.
91. Singh-Miller NE, Marzari N. Surface energies, work functions, and surface relaxations of low-index metallic surfaces from first principles. Physical Review B. 2009;80(23):235407.
92. De Boer FR, Mattens W, Boom R, Miedema A, Niessen A. Cohesion in metals. 1988.
93. Mittendorfer F, Eichler A, Hafner J. Structural, electronic and magnetic properties of nickel surfaces. Surface Science. 1999;423(1):1-11.
94. Mills K, Su Y. Review of surface tension data for metallic elements and alloys: Part 1–Pure metals. International Materials Reviews. 2006;51(6):329-51.
95. Aghemenloh E, Idiodi JOA, Azi SO. Surface energies of hcp metals using equivalent crystal theory. Computational Materials Science. 2009;46(2):524-30.
96. Methfessel M, Hennig D, Scheffler M. Trends of the surface relaxations, surface energies, and work functions of the 4d transition metals. Physical Review B. 1992;46(8):4816.
97. Zólyomi V, Vitos L, Kwon S, Kollár J. Surface relaxation and stress for 5d transition metals. Journal of Physics: Condensed Matter. 2009;21(9):095007.
98. Skriver HL, Rosengaard N. Surface energy and work function of elemental metals. Physical Review B. 1992;46(11):7157.
99. Tyson W, Miller W. Surface free energies of solid metals: Estimation from liquid surface tension measurements. Surface Science. 1977;62(1):267-76.
100. Tran R, Xu Z, Radhakrishnan B, Winston D, Sun W, Persson KA, et al. Surface energies of elemental crystals. Scientific data. 2016;3:160080.
101. Lozovoi AY, Alavi A. Reconstruction of charged surfaces: General trends and a case study of Pt (110) and Au (110). Physical Review B. 2003;68(24):245416.
102. Wolfschmidt H, Paschos O, Stimming U. Hydrogen reactions on nanostructured surfaces. Fuel cell science: theory, fundamentals, and biocatalysis: John Wiley & Sons, Inc. Hoboken, NJ, USA; 2010. p. 1-70.
103. Srinivasan S. Electrode/electrolyte interfaces: Structure and kinetics of charge transfer. Fuel Cells: Springer; 2006. p. 27-92.
104. Takigawa I, Shimizu K-i, Tsuda K, Takakusagi S. Machine-learning prediction of the d-band center for metals and bimetals. RSC advances. 2016;6(58):52587-95.
105. Bai Y, Kirvassilis D, Xu L, Mavrikakis M. Atomic and molecular adsorption on Ni(111). Surface Science. 2019;679:240-53.
106. Zhang L, Qiao L, Bligaard T, Su Y. A first-principle study of H adsorption and absorption under the influence of coverage. Applied Surface Science. 2018;457:280-6.
107. Ferrin P, Kandoi S, Nilekar AU, Mavrikakis M. Hydrogen adsorption, absorption and diffusion on and in transition metal surfaces: A DFT study. Surface Science. 2012;606(7):679-89.
108. Kresse G, Hafner J. First-principles study of the adsorption of atomic H on Ni (111),(100) and (110). Surface science. 2000;459(3):287-302.
109. Herron JA, Tonelli S, Mavrikakis M. Atomic and molecular adsorption on Pd (111). Surface science. 2012;606(21-22):1670-9.
110. Nie J, Xiao H, Zu X. First-principles study of H adsorption on and absorption in Cu (1 1 1) surface. Chemical physics. 2006;321(1-2):48-54.
111. Bhatia B, Sholl DS. Chemisorption and diffusion of hydrogen on surface and subsurface sites of flat and stepped nickel surfaces. The Journal of chemical physics. 2005;122(20):204707.
112. Greeley J, Mavrikakis M. Surface and subsurface hydrogen: adsorption properties on transition metals and near-surface alloys. The Journal of Physical Chemistry B. 2005;109(8):3460-71.

113. Watson GW, Wells RP, Willock DJ, Hutchings GJ. A comparison of the adsorption and diffusion of hydrogen on the {111} surfaces of Ni, Pd, and Pt from density functional theory calculations. The Journal of Physical Chemistry B. 2001;105(21):4889-94.
114. Mavrikakis M, Rempel J, Greeley J, Hansen LB, Nørskov JK. Atomic and molecular adsorption on Rh (111). The Journal of chemical physics. 2002;117(14):6737-44.
115. Santiago-Rodriguez Y, Herron JA, Curet-Arana MC, Mavrikakis M. Atomic and molecular adsorption on Au (111). Surface science. 2014;627:57-69.
116. Chen Q, Svenum I-H, Gavrilovic L, Chen D, Blekkan EA. Effect of trace potassium on hydrogen adsorption and dissociation on hcp cobalt: A density functional theory study. Surface Science. 2019;681:24-31.
117. Xu L, Lin J, Bai Y, Mavrikakis M. Atomic and molecular adsorption on Cu (111). Topics in Catalysis. 2018;61(9-11):736-50.
118. Krekelberg WP, Greeley J, Mavrikakis M. Atomic and molecular adsorption on Ir (111). The Journal of Physical Chemistry B. 2004;108(3):987-94.
119. Vasić D, Ristanović Z, Pašti I, Mentus S. Systematic DFT-GGA study of hydrogen adsorption on transition metals. Russian Journal of Physical Chemistry A. 2011;85(13):2373-9.
120. Liu C, Zhu L, Wen X, Yang Y, Li Y-W, Jiao H. Hydrogen Adsorption on Ir (111), Ir (100) and Ir (110)—Surface and Coverage Dependence. Surface Science. 2020;692:121514.
121. Zhang H, Li W-X. First-principles investigation of surface and subsurface H adsorption on Ir (111). The Journal of Physical Chemistry C. 2009;113(51):21361-7.
122. Shi Q, Sun R. Adsorption manners of hydrogen on Pt(100), (110) and (111) surfaces at high coverage. Computational and Theoretical Chemistry. 2017;1106:43-9.
123. Ford DC, Xu Y, Mavrikakis M. Atomic and molecular adsorption on Pt (1 1 1). Surface Science. 2005;587(3):159-74.
124. Kristinsdóttir L, Skúlason E. A systematic DFT study of hydrogen diffusion on transition metal surfaces. Surface science. 2012;606(17-18):1400-4.
125. Gómez EdV, Amaya-Roncancio S, Avalle LB, Linares DH, Gimenez MC. DFT study of adsorption and diffusion of atomic hydrogen on metal surfaces. Applied Surface Science. 2017;420:1-8.
126. Qin C, Whitten JL. Adsorption of O, H, Oh, and H2o on Ag (100). The Journal of Physical Chemistry B. 2005;109(18):8852-6.
127. Lerch D, Klein A, Schmidt A, Müller S, Hammer L, Heinz K, et al. Unusual adsorption site of hydrogen on the unreconstructed Ir (100) surface. Physical Review B. 2006;73(7):075430.
128. Jiang Z, Wang B, Fang T. Adsorption and dehydrogenation mechanism of methane on clean and oxygen-covered Pd (100) surfaces: A DFT study. Applied Surface Science. 2014;320:256-62.
129. Johnson DF, Carter EA. Hydrogen in tungsten: Absorption, diffusion, vacancy trapping, and decohesion. Journal of Materials Research. 2010;25(2):315-27.
130. Xu L, Kirvassilis D, Bai Y, Mavrikakis M. Atomic and molecular adsorption on Fe(110). Surface Science. 2018;667:54-65.
131. Bai Y, Chen BW, Peng G, Mavrikakis M. Density functional theory study of thermodynamic and kinetic isotope effects of H 2/D 2 dissociative adsorption on transition metals. Catalysis Science & Technology. 2018;8(13):3321-35.
132. Weststrate CJ, Mahmoodinia M, Farstad MH, Svenum I-H, Strømsheim MD, Niemantsverdriet JW, et al. Interaction of hydrogen with flat (0001) and corrugated (11–20) and (10–12) cobalt surfaces: Insights from experiment and theory. Catalysis Today. 2020;342:124-30.
133. Herron JA, Tonelli S, Mavrikakis M. Atomic and molecular adsorption on Ru (0001). Surface science. 2013;614:64-74.

134. López-Moreno S, Romero A. Atomic and molecular oxygen adsorbed on (111) transition metal surfaces: Cu and Ni. The Journal of chemical physics. 2015;142(15):154702.
135. Ford DC, Nilekar AU, Xu Y, Mavrikakis M. Partial and complete reduction of O2 by hydrogen on transition metal surfaces. Surface Science. 2010;604(19-20):1565-75.
136. Miller SD, İnoğlu N, Kitchin JR. Configurational correlations in the coverage dependent adsorption energies of oxygen atoms on late transition metal fcc (111) surfaces. The Journal of chemical physics. 2011;134(10):104709.
137. Miller SD, Kitchin JR. Relating the coverage dependence of oxygen adsorption on Au and Pt fcc (1 1 1) surfaces through adsorbate-induced surface electronic structure effects. Surface science. 2009;603(5):794-801.
138. Todorova M, Reuter K, Scheffler M. Oxygen Overlayers on Pd(111) Studied by Density Functional Theory. The Journal of Physical Chemistry B. 2004;108(38):14477-83.
139. Reuter K, Stampfl C, Ganduglia-Pirovano MV, Scheffler M. Atomistic description of oxide formation on metal surfaces: the example of ruthenium. Chemical Physics Letters. 2002;352(5-6):311-7.
140. Chen BW, Kirvassilis D, Bai Y, Mavrikakis M. Atomic and molecular adsorption on Ag (111). The Journal of Physical Chemistry C. 2018;123(13):7551-66.
141. Boungou CC, N'Dollo M, Bouka-Pivoteau GB, Moussounda PS, Dintzer T. Density functional studies of the adsorption of OCN and coadsorption of O and CN on Ag(001) surface. Computational Condensed Matter. 2020;22:e00446.
142. Duan X, Warschkow O, Soon A, Delley B, Stampfl C. Density functional study of oxygen on Cu(100) and Cu(110) surfaces. Physical Review B. 2010;81(7):075430.
143. Hansen E, Neurock M. Predicting lateral surface interactions through density functional theory: application to oxygen on Rh(100). Surface Science. 1999;441(2):410-24.
144. Eichler A, Hafner J. NO reduction by CO on the Pt (100) surface: a density functional theory study. Journal of Catalysis. 2001;204(1):118-28.
145. Ge Q, Hu P, King D, Lee M-H, White J, Payne M. Site symmetry dependence of repulsive interactions between chemisorbed oxygen atoms on Pt {100}-(1× 1). The Journal of chemical physics. 1997;106(3):1210-5.
146. Johnson K, Ge Q, Titmuss S, King D. Unusual bridged site for adsorbed oxygen adatoms: Theory and experiment for Ir {100}–(1× 2)–O. The Journal of Chemical Physics. 2000;112(23):10460-6.
147. Deskins NA, Lauterbach J, Thomson KT. Lifting the Pt {100} surface reconstruction through oxygen adsorption: A density functional theory analysis. The Journal of chemical physics. 2005;122(18):184709.
148. Liu DJ, Evans JW. Interactions between oxygen atoms on Pt (100): implications for ordering during chemisorption and catalysis. ChemPhysChem. 2010;11(10):2174-81.
149. Cao W. Using and validation of the DFT method for oxygen adsorbed on the iron (100) surface. Mineral Processing and Extractive Metallurgy. 2010;119(2):67-70.
150. Błoński P, Kiejna A, Hafner J. Theoretical study of oxygen adsorption at the Fe (1 1 0) and (1 0 0) surfaces. Surface science. 2005;590(1):88-100.
151. Scheijen FJE, Niemantsverdriet JW, Curulla-Ferré D. Adsorption, Desorption, and Dissociation of CO on Tungsten(100), a DFT Study. The Journal of Physical Chemistry C. 2008;112(19):7436-44.
152. Scheijen FJE, Niemantsverdriet JW, Ferré DC. Density Functional Theory Study of CO Adsorption and Dissociation on Molybdenum(100). The Journal of Physical Chemistry C. 2007;111(36):13473-80.
153. Ossowski T, Kiejna A. Oxygen adsorption on Fe (110) surface revisited. Surface Science. 2015;637:35-41.
154. Stöhr M, Podloucky R, Müller S. Ab initio phase diagram of oxygen adsorption on W (110). Journal of Physics: Condensed Matter. 2009;21(13):134017.
155. Zhou Y, Zu XT, Nie J, Gao F. Adsorption of O on Mo (110) surface from first-principles calculation. The European Physical Journal B. 2009;67(1):27-34.
156. Ji Z, Li J-Q. Dissociative Adsorption of Carbon Monoxide on Mo(110): First-Principles Theory. The Journal of Physical Chemistry B. 2006;110(37):18363-7.

157. Petrova N, Yakovkin I. Density-functional and Monte Carlo study of O⁄Mo (110): structures and desorption. Physical Review B. 2007;76(20):205401.
158. Ma SH, Jiao ZY, Wang TX, Dai XQ. First-principles studies of oxygen chemisorption on Co(0001). Surface Science. 2014;619:90-7.
159. Huo C-F, Li Y-W, Wang J, Jiao H. Adsorption and Dissociation of CO as Well as CHx Coupling and Hydrogenation on the Clean and Oxygen Pre-covered Co(0001) Surfaces. The Journal of Physical Chemistry C. 2008;112(10):3840-8.
160. Stampfl C, Scheffler M. Theoretical study of O adlayers on Ru (0001). Physical Review B. 1996;54(4):2868.
161. Yao K, Yuan Z, Jin S, Chi Q, Liu B, Huang R, et al. Efficient hydrodeoxygenation of sulfoxides into sulfides under mild conditions using heterogeneous cobalt–molybdenum catalysts. Green Chemistry. 2020;22(1):39-43.
162. Lalsare A, Sivri A, Egan R, Vukmanovich RJ, Dumitrescu CE, Hu J. Biomass – Flare gas synergistic co-processing in the presence of carbon dioxide for the controlled production of syngas (H2:CO ~ 2 – 2.5). Chemical Engineering Journal. 2020;385:123783.
163. Olcese RN, Bettahar M, Petitjean D, Malaman B, Giovanella F, Dufour A. Gas-phase hydrodeoxygenation of guaiacol over Fe/SiO2 catalyst. Applied Catalysis B: Environmental. 2012;115-116:63-73.
164. Echeandia S, Arias P, Barrio V, Pawelec B, Fierro J. Synergy effect in the HDO of phenol over Ni–W catalysts supported on active carbon: Effect of tungsten precursors. Applied Catalysis B: Environmental. 2010;101(1-2):1-12.
165. Hintze JL, Nelson RD. Violin plots: a box plot-density trace synergism. The American Statistician. 1998;52(2):181-4.
166. Nanba Y, Koyama M. NO Adsorption on 4d and 5d Transition-Metal (Rh, Pd, Ag, Ir, and Pt) Nanoparticles: Density Functional Theory Study and Supervised Learning. The Journal of Physical Chemistry C. 2019;123(46):28114-22.
167. Nakagawa Y, Tomishige K. Total hydrogenation of furan derivatives over silica-supported Ni–Pd alloy catalyst. Catalysis Communications. 2010;12(3):154-6.
168. Stanković M, Krstić J, Gabrovska M, Radonjić V, Nikolova D, Lončarević D, et al. Supported Nickel-Based Catalysts for Partial Hydrogenation of Edible Oils. New Advances in Hydrogenation Processes: Fundamentals and Applications. 2017:131.
169. Resende KA, Braga AH, Noronha FB, Hori CE. Hydrodeoxygenation of phenol over Ni/Ce1-xNbxO2 catalysts. Applied Catalysis B: Environmental. 2019;245:100-13.
170. Banerjee A, Mushrif SH. Reaction Pathways for the Deoxygenation of Biomass-Pyrolysis-Derived Bio-oil on Ru: A DFT Study using Furfural as a Model Compound. ChemCatChem. 2017;9(14):2828-38.
171. Honkela ML, Björk J, Persson M. Computational study of the adsorption and dissociation of phenol on Pt and Rh surfaces. Physical Chemistry Chemical Physics. 2012;14(16):5849-54.
172. Hensley AJR, Wang Y, McEwen J-S. Adsorption of phenol on Fe (110) and Pd (111) from first principles. Surface Science. 2014;630:244-53.
173. Huynh TM, Armbruster U, Kreyenschulte CR, Nguyen LH, Phan BM, Nguyen DA, et al. Understanding the performance and stability of supported Ni-Co-based catalysts in phenol HDO. Catalysts. 2016;6(11):176.
174. Zhang X, Zhang Q, Wang T, Ma L, Yu Y, Chen L. Hydrodeoxygenation of lignin-derived phenolic compounds to hydrocarbons over Ni/SiO2–ZrO2 catalysts. Bioresource technology. 2013;134:73-80.
175. Bunch AY, Ozkan US. Investigation of the reaction network of benzofuran hydrodeoxygenation over sulfided and reduced Ni–Mo/Al2O3 catalysts. Journal of catalysis. 2002;206(2):177-87.

Supplementary material

Supplementary material can be used for supporting data sets, movies, figures and tables, and any other supporting material. The main article, however, should stand on its own merit. Where possible, supplementary material should be combined into one Word document or PDF. A template is available here.